Time and Phase Synchronization of a Broadband Multistatic Imaging Radar Network using Non-Cooperative Signals

Fabian Hochberg, Matthias Jirousek, Simon Anger, Markus Peichl, *Member, IEEE,*
and Thomas Zwick *Fellow, IEEE*

***Abstract*—High resolution multistatic imaging radar systems pose significant challenges to the employed synchronization schemes, as such radar networks need to operate coherently. Especially high resolution systems operating at a high center frequency push the required synchronization requirements into the single-digit picosecond regime. Within the project Imaging of Satellites in Space – Next Generation (IoSiS-NG), the task at hand is further challenged by the use of far baselines, where commonly seen approaches fail, as no line-of-sight (LOS) free-space propagation or wired method can be employed. In this paper, a robust synchronization method is presented that elevates well established GNSS based methods by about three orders of magnitude through the coordinated reception of non-cooperative (NC) signals at all participating nodes. Exploiting the identical signal payload at all stations, the timing and phase differences of the nodes can be tracked and corrected in the post-processing stage. Here, we demonstrate our newly developed algorithm, simulative studies as well as real-world experiments using satellite broadcast television (TV) signals as NC signals to synchronize a high-resolution imaging radar achieving a timing standard deviation of less than 1.8 ps and a phase coherence for the X-band radar of less than 2° allowing interferometric or tomographic imaging principles to be used.**

***Index Terms*—ISAR, synchronization, non-cooperative signals, multistatic radar, timing, signal processing.**

I. INTRODUCTION

RECENT research in the SAR and ISAR community clearly shows a trend towards new multistatic operations for interferometric and tomographic imaging systems [1]–[5]. This inevitably requires the need for high-performance synchronization techniques to coherently operate the sensor network. As the SAR principle relies on the phase of the reflected signal, a tight phase coupling in a multistatic system is required. Especially with interferometric systems, synchronization errors contribute substantially to the expected system performance [6]. A commonly seen approach to synchronize such a system is to use a direct line-of-sight (LOS) radio frequency (RF), optical or cable link between the participating nodes in the network [7], [8]. Additionally, the transmit radar waveform itself can be used for synchronization, if it is received at the remote nodes separately to the echo [3], [9]. Also in the context of SAR, data driven approaches can also be used, as is shown in [10]–[12]. Additionally, in the automotive sector, where strong multipath effects are present, coherent radar networks are also part of active research [13]. Here, data-driven approaches using a cooperative approach to jointly solve the synchronization task are also investigated. Developing new synchronization schemes based on global navigation satellite systems (GNSSs) are also part of current research, which rely on the carrier phase estimations of the GNSS signals [14], [15].

This work is related to the IoSiS-NG project, where a multistatic system to image objects in Earth's orbit is going to be set up [16]. The sensor network is composed of a single radar transmitter with a colocated receiver and multiple remote receive-only stations. With this system, the goal is to gather bistatic signatures, or three-dimensional pieces of information on objects in space. In order to be able to achieve the significant bistatic angle required for this system, baseline lengths of dozens of kilometers are required and thus pose significant requirements on the employed synchronization scheme. Such large baselines render any free-space propagation of a synchronization signal (RF or optical) impractical, as the topography and Earth's curvature hinder a LOS connection. Furthermore, a cable connection is not possible to populate through inhabited areas, and as this system should enable research into higher operational frequencies up to the millimeter wave regime, synchronization using GNSS signals becomes unfeasible, as tight phase coupling becomes challenging or impossible to achieve.

With those presented challenges, a different approach to synchronize multiple receiver nodes must be taken. This work presents a novel wireless synchronization technique for time and phase transfer using non-cooperative (NC) signals.

Other works like [17], [18] have also attempted synchronization using NC signals by the use of time of arrival (ToA) or time difference of arrival (TDoA) measurements. The work presented here interprets the approach differently, as we may not neglect the local oscillator (LO) phase relationship between the participating nodes. In order to be applicable to our ISAR system, we investigated the specifics of the NC signal reception in more detail and found an innovative solution using moderate hardware costs, as the fine synchronization is not physically achieved in the hardware system. Moreover, this synchronization approach does not aim for an absolute time synchronization to a global time frame, which is assumed to be coarsely achieved through common methods such as GNSS based methods. The work presents the fine synchronization to obtain picosecond level relative timing and phase estimates to

Date of current version 13 January 2026. This work was supported by the Bavarian Ministry of Economic Affairs, Regional Development and Energy within the scope of the IoSiS-NG project. (Corresponding author: Fabian Hochberg.)

Fabian Hochberg, Matthias Jirousek, Simon Anger and Markus Peichl are with the Microwaves and Radar Institute, German Aerospace Center (DLR), 82234 Weßling, Germany (e-mail: fabian.hochberg@dlr.de; matthias.jirousek@dlr.de; simon.anger@dlr.de; markus.peichl@dlr.de).

Thomas Zwick is with the Institute of Radio Frequency Engineering and Electronics, Karlsruhe Institute of Technology (KIT), 76131 Karlsruhe, Germany (e-mail: thomas.zwick@kit.edu).

Article published by IEEE: https://doi.org/10.1109/TRS.2026.3654640
Cite as: F. Hochberg, M. Jirousek, S. Anger, M. Peichl and T. Zwick, "Time and Phase Synchronization of a Broadband Multistatic Imaging Radar Network Using Non-Cooperative Signals," in *IEEE Transactions on Radar Systems*, vol. 4, pp. 373-386, 2026, doi: 10.1109/TRS.2026.3654640.

correct the recorded radar data in the post-processing stage, which is about three orders of magnitude better than regular GNSS-based synchronization.

We structured this paper as follows. In Section II the system concept and the signal model of the received signals, as well as the proposed synchronization scheme are described, whereas in Section III we delve into the developed algorithm to retrieve the phase and timing correction signals needed to establish a coherent radar. Next, in Section IV the simulative studies are shown before in Section V the experimental setup and results are described and demonstrated, verifying the proposed synchronization scheme. Finally, in Section VI the key findings are summarized and future studies for further investigations are proposed.

A Note on the notation used in this paper: This work describes a system with multiple identical remote nodes and a singular base node. A total of N nodes are present, the n-th node is addressed via the subscript n. As each node will run on its own base clock, the superscript ℓ is used to indicate a local time frame, meaning the values denoted with ℓ are referring to the internal clock readout values of a node. Due to drifts and offsets, the same time value for t^ℓ in the internal clocks will not necessarily be the same time instance on all units relative to a global time frame. Using this formulation, t_n^ℓ is the local clock for the n-th node in the system, on which the node can act on.

The non-cooperative (NC) signal, which will be used for synchronization, will be denoted with the short form subscript nc.

II. System and Signal Model

Multistatic high resolution imaging radar systems pose significant requirements on the time stability and jitter performance of the system [6]. To regain the highest performance metrics a proper system and signal model is mandatory to adequately describe the occurring real-world effects when operating with multiple participating nodes.

A. Node design and system model

A participating node can be described by the simplified block diagram in Fig. 1, where the remote nodes are only equipped with receiving hardware. The base node, which is denoted with the index 0, is also capable of transmitting the radar signal. To maintain the flexibility needed in the radar image formulation and synchronization, a frequency modulated pulse radar system is used, which samples the received signals in the time domain. A single acquisition for the imaging task will consist of a set of acquired pulses and the same idea is applied for the NC signal receiver. The NC signal will be acquired in P pulses of pulsed acquisition intervals (PAIs). The synchronization task at hand is to synchronize the remote nodes to the base node.

To model the occurring differences in time and phase in the system, a timed description is needed. Firstly, each node will have its own base clock to derive the local time of the node resulting in a local clock value t_n^ℓ. As the local clock readout value is not necessarily the true time, a unified mathematical model is needed to describe the system as a whole. We introduce the time globalization operator $\mathcal{T}_n(\cdot)$:

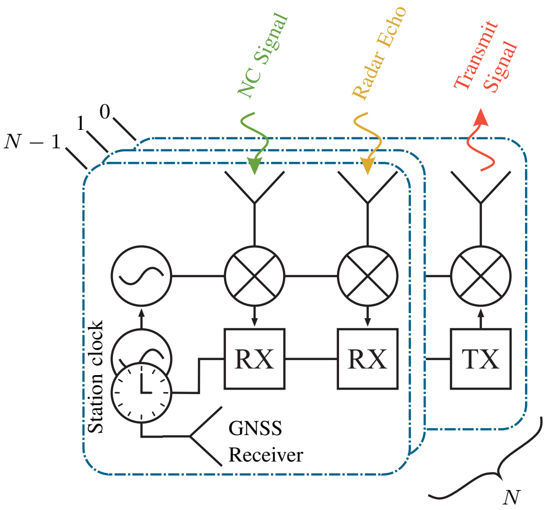

Fig. 1: Schematic radar node design, with a receiver for the NC signal on the left (green), and for the radar signal in the middle (yellow). The base node 0 is also equipped with the radar transmitter on the right (red). Further analog hardware is omitted for simplicity, and the system is composed of N nodes.

$$t = \mathcal{T}_n(t^\ell)\,, \tag{1}$$

where the global time frame is denoted with t and the local clock value with t^ℓ.

One often comes across a linear model for the time transfer equation from the local clock to the global time frame [19]. However, the validity is seldomly questioned. As the local time of a node is rooted in the progressing oscillations of a base clock oscillator, a strict linear relationship is not expected to hold true for all times. Real-world oscillators inevitably exhibit a drift due to aging or changing environmental conditions [20]. Thus, a more detailed description of the local time can be made:

$$t_n^\ell = \int \frac{f_n^i(t)}{f_0}\,\mathrm{d}t + \Delta t_{n,0} := \mathcal{T}_n^{-1}(t) \tag{2}$$

Where $f_n^i(t)$ is the time-varying instantaneous frequency of the oscillator and f_0 is its nominal frequency. Since $f_n^i(t) > 0$ holds, (2) is a bijective mapping that uniquely assigns a timestamp in the local time frame to each true global point in time. This way, the time localization operation $\mathcal{T}_n^{-1}$ can be defined as seen in (2). As the function is bijective, one can see that the inverse, the time globalization operation from (1) must exist. Evidently, this operator serves a simplification for the following signal description, as the realization of the offset and drift of node n are encapsulated in the operator itself. By doing so, the description for a supposedly simultaneous event at all stations at time t^ℓ, can be denoted with $\mathcal{T}_n(t^\ell)$, which is different for each node n. Using the model from (2), also coupled or disciplined oscillators can be described to model the local times of each node.

In addition, it is not sufficient to only consider the timing of a node, as the phase relationship must be taken into account in the frequency conversion stage of each node. The LO signal is referenced to the station clock oscillator by the use of a phase-locked loop (PLL) [21]. Moreover, for imaging radar applications, the absolute phase of the oscillator is of uttermost importance, as it defines the achievable azimuth focusing [22]. The LO phase noise outside the loop filter bandwidth is determined by the internal oscillator of the PLL, which adds uncorrelated phase noise within a node and degrades the received signal coherence [21]. Also, as PLLs are control loops, non-deterministic phase drifts outside the loop-filters bandwidth around the reference phase are present. To achieve a high phase synchronization between nodes, these effects may not be neglected.

The LO signal of node n can be modelled with

$$l_n(t) = A \exp\left(\mathrm{j}\left(2\pi f_{n,\mathrm{LO}} t + \varphi_{n,0} + \varsigma_n(t)\right)\right), \tag{3}$$

where A is the constant amplitude (amplitude variations are neglected in this work, $A = 1$ can be assumed), $f_{n,\mathrm{LO}}$ is the local oscillator frequency, $\varphi_{n,0}$ is an initial phase offset, and ς_n is a realization of a colored phase noise process, whose characteristics are mainly described by the PLL in use [21]. It should be noted that the value of $f_{n,\mathrm{LO}}$ is the time-variable frequency as seen when measured against the global time reference. Measuring $f_{n,\mathrm{LO}}$ with respect to t_n^{ℓ} would yield its nominal value, unaffected by base clock drifts.

As can be seen in the node design in Fig. 1, all frequency conversion stages of a node are using the same LO signal. With that, the goal is to exploit the fact that all signals undergo the same frequency conversion, resulting in the same phase drifts at all receivers in a node. Notably, the operational frequencies of the NC signal and the radar application should be close to each other to achieve the baseband or intermediate frequency (IF) conversion using the identical LO signal. Alternatively, if the two frequency ranges are not close together, a fixed frequency coupling (multiplication or division stages) should be used, to maintain a locked phase relationship between the radar receiver and NC signal receiver. If these conditions cannot be met, and two different PLLs need to be used to generate the down conversion of the two receiver chains, phase noise contributions outside the loop-filters bandwidth cannot be captured using the method presented here. For now, we will focus our attention to the case where the same LO signal can be used for both receivers.

As the base node, where the transmitter is located, also receives the NC signal, it can serve as a reference signal for comparing the remote reception of the NC signal. Since the base node operates like a monostatic system, it maintains coherence with the transmitter. Consequently, if the remote nodes are synchronized to the base node's receiver, they are inherently synchronized to the transmitter as well. Therefore, timing and phase errors determined through signal processing based on the NC signals can be applied to the radar signal, resulting in a coherent radar system. To enable this functionality, all nodes must be coarsely synchronized, requiring their timing to be aligned such that their reception windows overlap during a PAI. This initial synchronization can be achieved, for instance, by utilizing GNSS-disciplined oscillators.

B. *Non-cooperative signal reception*

All participating nodes receive a NC signal on their secondary receiver chain, which will be used for determining the time and phase offsets between the nodes. This NC signal is conveniently a broadband modulated signal that can be continuously received at all participating nodes, which can be described by

$$s_{\mathrm{nc}}(t) = m(t) \cdot \exp(\mathrm{j}2\pi f_{\mathrm{nc,c}} t), \tag{4}$$

where $m(t)$ is the modulated baseband signal, and $f_{\mathrm{nc,c}}$ is the RF carrier frequency of the signal. This signal at the antenna of node n can be described by

$$s_{n,\mathrm{nc}}(t) = h_{\mathrm{nc}\to n}(t) * s_{\mathrm{nc}}(t) \tag{5}$$

with $h_{\mathrm{nc}\to n}(t)$ being the channel from the origin of the NC signal towards the receiving antenna of node n. For the scope of this paper, free space propagation between the origin of the NC signal and node n is assumed resulting in

$$h_{\mathrm{nc}\to n} = D_n \cdot \delta(t - \tau_{\mathrm{nc}\to n}). \tag{6}$$

Here, D_n is the signal attenuation factor and $\tau_{\mathrm{nc}\to n}$ the propagation delay between the NC signal source and node n as defined by

$$\tau_{\mathrm{nc}\to n} = \frac{\|\vec{x}_{\mathrm{nc}} - \vec{x}_n\|}{\mathrm{c}_0}, \tag{7}$$

with $\vec{x}$ being the geometrical position vector of the origin of the NC signal and node n respectively, and c_0 being the speed of light. For now, only stationary scenarios are considered. The channel given in (6) neglects multipath effects, which is an assumption that may not hold true for all scenarios, especially in grounded applications where urban canyons might be present. In order to establish the working principle of the proposed scheme, we stick to this simplified channel model here and reiterate on the issue later in Section VI.

Using the descriptions from above, the received down converted NC signal at node n can be written as

$$\begin{aligned} r_{n,\mathrm{nc}}(t) &= \left(h_{\mathrm{nc}\to n}(t) * s_{n,\mathrm{nc}}(t)\right) \cdot l_n^*(t) + w_n(t) \\ &= D \cdot m(t - \tau_{\mathrm{nc}\to n}) \cdot \exp\left(\mathrm{j}2\pi f_{\mathrm{nc,c}}(t - \tau_{\mathrm{nc}\to n})\right) \\ &\quad \cdot \exp\left(-\mathrm{j}\left(2\pi f_{n,\mathrm{LO}} t + \varphi_{n,0} + \varsigma_n(t)\right)\right) + w_n(t). \end{aligned} \tag{8}$$

When the signal from (8) enters the node n it is localized to the local time frame and superimposed with white Gaussian receiver noise w_n. Comparing the NC signal for every time instance at two nodes 1 and 2 results in

- a time offset caused by a geometric separation $\tau_{\mathrm{nc}\to 1} - \tau_{\mathrm{nc}\to 2}$ and local time frame differences $\mathcal{T}_1(t^{\ell}) - \mathcal{T}_2(t^{\ell})$.
- a frequency offset caused by two oscillators $f_{1,\mathrm{LO}} - f_{2,\mathrm{LO}}$.
- a phase offset caused by different initial phase offsets and phase noise realizations $(\varphi_{1,0} + \varsigma_1(t)) - (\varphi_{2,0} + \varsigma_2(t))$.

By design, all mentioned offsets are small and slowly evolving with time, and the goal is to estimate their values.

The digitally sampled signal, which is used for digital post-processing, is defined by the local time frame. Each node will sample at the predefined local time instances of

$$t^{\ell}_{n,\mathrm{s}}\,[k] = \frac{k \bmod K}{f^{\ell}_{\mathrm{s}}} + \left\lfloor \frac{k}{K} \right\rfloor \cdot \mathrm{PRI}^{\ell} + t^{\ell}_{n,0_{\mathrm{NC}}}\ , \qquad (9)$$
$$\text{with } k \in \{0, \dots, P \cdot K - 1\}\ ,$$

where k is the sample index, K is the number of samples per pulse, P is the number of pulses acquired, mod is the modulo operator, f^{ℓ}_{s} is the nominal sample rate, $\lfloor\cdot\rfloor$ is the flooring operator, and PRI^{ℓ} is the nominal pulse-repetition interval (PRI). To compensate for the geometrical disposition of the nodes, each node will need to start at slightly different times ($t^{\ell}_{n,0_{\mathrm{NC}}}$) such that the recorded signal vector contains the same signal payload at all nodes. The record start time $t^{\ell}_{n,0_{\mathrm{NC}}}$ can be pre-computed and is used for the reduction of the time offset $\tau_{\mathrm{nc}\to 1} - \tau_{\mathrm{nc}\to 2}$ in the received signal vectors. One can use

$$t^{\ell}_{0,0_{\mathrm{NC}}} = T_0 \text{ and} \qquad (10)$$
$$t^{\ell}_{n,0_{\mathrm{NC}}} = T_0 + \tau_{\mathrm{nc}\to n} - \tau_{\mathrm{nc}\to 0} \qquad (11)$$

for the start times, where T_0 is the measurement start time. Obviously, the computed value of (11) will not be accurate enough for absolute time synchronization, as the location of the NC signal's origin is not excatly known. However, a rough position estimate for the NC signal's origin is still needed, if the geometrical disposition of the radar nodes leads to a delay spread ($\tau_{\mathrm{nc}\to n} - \tau_{\mathrm{nc}\to 0}$) in the order of the PAI duration. Usually, a coarse range delay estimate in the order of few microseconds will suffice, it is only needed to ensure identical signal payload reception.

The received signal (8) is sampled at the true time instances

$$t_{n,\mathrm{s}}\,[k] = \mathcal{T}_n\left(t^{\ell}_{\mathrm{s}}\,[k]\right)\ , \qquad (12)$$

where the individual local time offset and drift is embedded in the time globalization operator $\mathcal{T}_n$ of node n.

III. SYNCHRONIZATION ALGORITHM

Our newly proposed synchronization scheme is applied in the post-processing stage once the acquisition is done. The entirety of the received signals can be described by the dataset $\{\mathbf{R}_n\,[p,m]\}_{n=0}^{N-1}$, where each $\mathbf{R}_n \in \mathbb{C}^{P\times K}$. This way, the continuous NC signal stream of each node is sorted in pulsed segments (PAIs) with a total of P pulses

$$\mathbf{R}_n\,[p,m] = r_n\left(t_{n,\mathrm{s}}\,[p\cdot K + m]\right) \qquad (13)$$
$$\text{with } p \in \{0,\dots,P-1\}\ ,$$
$$\text{and } m \in \{0,\dots,K-1\}\ .$$

To achieve synchronization, the goal is to estimate the timing and phase differences between the base node 0 and all other participating nodes. It is not of interest, to synchronize the base node to a global time frame, as its local timing and LO is determining the transmitted signal. Coherence is only needed relative to the transmitted signal. In order to simplify the following formulation, only the synchronization of node n to the base node 0 is depicted. It is understood that it needs to be done for each node $n \in \{1,\dots,N-1\}$. Furthermore, it is evident, that the computational effort for multiple remote nodes scales with $\mathcal{O}(N)$, as the algorithm is executed pairwise for each remote node n to the base node 0.

The estimation process is performed in two sequential steps: firstly, the timing offsets and their respective rates are determined, and secondly the frequency and phase errors are estimated. The complete synchronization algorithm can be seen in Algorithm 1.

A. Timing estimation

To obtain the timing estimates to correct for relative clock offsets and drifts, the recorded NC signal vectors are compared in time. The recorded signal vectors of all stations will span the same number of samples, but due to a possibly existing sampling rate offset, they may not span the same duration. The magnitude of this effect is addressed in appendix A, and for now neglected. This way, we can assume there exist a single time offset $\Delta t_{n\to 0}$ between the base node and remote nodes, which varies on a PAI to PAI basis.

Consequently, the task at hand is to estimate the time offsets between the NC signal at the node n and the base node 0. We assume that the NC signal behaves pseudo-random, i.e. has a distinct peak in its autocorrelation function (ACF), and can be described with a quasi-rectangular power spectral density (PSD) function. These properties do not put too stringent constraints on the selectable NC signals, as modulated broadcast data streams usually behave in such a way [23, Chapter 2.3].

A time estimate can be readily obtained by a cross-correlation followed by suitable peak finding step. An efficient TDoA estimate is presented in [24] by applying a nonlinear least-squares fit that employs a sinc function kernel. Following the notation from [24], the estimator performs a Gauss-Newton optimization to minimize the cost function

$$C = \sum_{i=0}^{2} \left(y_i - f(i-1,\boldsymbol{\lambda})\right)^2 \qquad (14)$$
$$\text{with } \boldsymbol{\lambda} = [\lambda_0, \lambda_1, \lambda_2]^T\ , \qquad (15)$$
$$f(x,\boldsymbol{\lambda}) = \lambda_0 \operatorname{sinc}\left((x-\lambda_1)\lambda_2\right)\ , \qquad (16)$$
$$y_i = |d[m_{\mathrm{pk}} - 1 + i]| \quad i \in \{0,1,2\}\ . \qquad (17)$$

Here $d[\cdot]$ is the cross correlation function between the signals $\boldsymbol{R}_n[p,:]$ and $\boldsymbol{R}_0[p,:]$ for PAI p and the remote node n to the base node 0, and m_{pk} is the peak index of said correlation function. The minimal cost function is obtained by the vector $\hat{\boldsymbol{\lambda}}$, thus the final timing estimate is obtained with

$$\Delta\hat{t}_{n\to 0} = \frac{m_{\mathrm{pk}} + \hat{\lambda}_1}{f^{\ell}_{\mathrm{s}}}\ . \qquad (18)$$

It should be noted, that the estimated time difference is not directly the present clock offset, as its value is modified by the propagation delay difference and the local sampling time offsets. Meaning, the first estimate will be composed of

$$\Delta\hat{t}_{n\to 0}[0] = \mathcal{T}_n(t^{\ell}_{n,0_{\mathrm{NC}}}) - \mathcal{T}_0(t^{\ell}_{0,0_{\mathrm{NC}}}) + \tau_{\mathrm{nc}\to 0} - \tau_{\mathrm{nc}\to 1}\,. \qquad (19)$$

This estimate describes the timing offset in the sampled signal vectors, not directly the node's timing errors.

Once the timing is estimated from the given vectors, one can shift the node's signal vector such that there remains no time difference between node n and the base node's NC signal vectors. The shifting can be done with simple FFT based methods. As such a method shifts the signal cyclically, $\lceil m_{\mathrm{pk}} + \hat{\lambda}_1 \rceil$ samples from the left or right need to be omitted from further consideration. The aligned data matrix will be denoted with $\boldsymbol{R}_{n,\leftrightarrow}[p,m]$ and will align the signals at the base station to a subsample level accuracy.

The gradient of the time offsets $\Delta\hat{t}_{n\to 0}[p]$ gives the instantaneous clock rate differences, as stationary scenarios are assumed, the only varying component of (19) is the local clock drift. As the LO signal is coupled to the station clock, a coarse estimate for the LO difference frequency can thus be made

$$\Delta\hat{f}^{(0)}[p] = f_{\mathrm{LO}}^{\ell} \cdot \nabla \Delta\hat{\boldsymbol{t}}_{n\to 0} \, , \tag{20}$$

which will be useful for the frequency and phase estimation step. In this case, the differentiation of the obtained time estimates for all PAIs $\Delta\hat{\boldsymbol{t}}_{n\to 0}$ is denoted with the nabla operator.

B. Phase estimation

With the vectors aligned, there remains no time offset. This allows a cancellation of the modulation payload $m(t)$ of the NC signal by an element-wise complex conjugate multiplication

$$\boldsymbol{S}_n[p,m] = \boldsymbol{R}_0[p,m] \odot \overline{\boldsymbol{R}}_{n,\leftrightarrow}[p,m] \, , \tag{21}$$

where $\odot$ is the Hadamard product operator and $\bar{\cdot}$ represents an element-wise complex conjugate. As the signal vectors align in time, the complex conjugate multiplication eliminates the signal payload and carrier phase form (8) as $\angle\{x \cdot x^*\} = 0$ holds for any $x \in \mathbb{C}$. The phase of $\boldsymbol{S}_n[p,m]$ is determined by

- the frequency offset $f_{1,\mathrm{LO}} - f_{2,\mathrm{LO}}$,
- the initial phase offsets $\varphi_{n,0} - \varphi_{0,0}$,
- a phase offset due to the propagation delay $2\pi \cdot (f_{n,\mathrm{LO}}\tau_{\mathrm{nc}\to\mathrm{n}} - f_{0,\mathrm{LO}}\tau_{\mathrm{nc}\to 0})$,
- a phase offset due to the different initial record start times $2\pi \cdot (f_{n,\mathrm{LO}}t_{n,0_{\mathrm{NC}}} - f_{0,\mathrm{LO}}t_{0,0_{\mathrm{NC}}})$,
- and noise components.

It now resides to estimate the frequency and phase of $\boldsymbol{S}_n[p,m]$, whose components we assume to be slowly evolving with time. As this work assumes a constant acquisition geometry, the phase contribution due to the propagation delay is assumed to be constant as well. All other components are not constant over the whole acquisition time, but are assumed to be constant within a single PAI. By design, $f_{n,\mathrm{LO}} - f_{0,\mathrm{LO}}$ is very small and only shows the instantaneous drift. The local clock is coupled to GNSS, which serves as the LO reference, resulting in the identical mean frequency of the LO signal, however, drifts and effects outside the time constant of the joint loop filter will be present and need to be corrected [21]. This means, the task to estimate the difference frequency is to estimate a frequency very close to the lower Nyquist boundary, which is inherently inaccurate [25, Chapter 3.11]. To combat this, the idea is not to estimate the changing frequency on a per-pulse basis, but rather to estimate the difference frequency over two (or more) consecutive pulses. This way, an accurate and precise estimate can be obtained. A sliding window can be used to select a total of W pulses to be used for the estimation. It should be noted, that a singular sinusoidal frequency estimation is performed over W pulses, which means it is important to choose W in accordance with the expected stability of the oscillators used.

Now it is once again useful to stop thinking about pulsed signals and rather think about the remaining difference signal matrix $\boldsymbol{S}_n[p,m]$ as a continuous non-equidistant sampled signal vector

$$s_n[k] = \boldsymbol{S}_n\left[\left\lfloor \frac{k}{K} \right\rfloor, k \bmod K\right] . \tag{22}$$

For the estimation process, a subset of samples $\mathscr{K}_p$ are used. To estimate the correction values for pulse p and window size W one can select the samples to use by

$$\mathscr{K}_p = \{K \cdot (p - \lfloor (W-1)/2 \rfloor), \ldots, K \cdot (p + \lfloor W/2 \rfloor)\} . \tag{23}$$

As the estimation task is to estimate a single sinusoid in a noisy signal vector, multiple estimation methods are possible. However, as the signal vector is non-equidistantly sampled, the estimation algorithm needs to be able to handle this without the need for a zero-filled equidistant signal vector. For example, a simple periodogram estimator as in (25) can be used, as the local timestamps for each sample can be used directly [25, Chapter 7.10]. There may exist more computationally efficient estimators, but a study on those is outside the scope of this work. To define the search space, the coarse frequency estimate $\Delta\hat{f}^{(0)}$ from (20) can be used as an initial guess. Using

$$\mathscr{R} = \left[\Delta\hat{f}^{(0)} - \frac{\mathrm{PRF}^{\ell}}{2}, \Delta\hat{f}^{(0)} + \frac{\mathrm{PRF}^{\ell}}{2}\right) \tag{24}$$

with PRF^{ℓ} being the configured pulse repetition frequency for the PAIs for the NC signal. The minimization given in (25) can be achieved by usual minimum search approaches such as the Nelder-Mead method [26]. Once the frequency offset per pulse is estimated, the phase offset can then be easily computed by (26).

$$\Delta\hat{f}_n[p] = \underset{f\in\mathscr{R}}{\arg\min}\left\{\frac{-1}{WK}\left|\sum_{k'\in\mathscr{K}_p} s_n[k'] \cdot \mathrm{e}^{-\mathrm{j}2\pi\cdot f\cdot t_{\mathrm{s}}^{\ell}[k']}\right|^2\right\} \tag{25}$$

$$\Delta\hat{\varphi}_n[p] = \angle\left\{\sum_{k'\in\mathscr{K}_p} s_n[k'] \cdot \mathrm{e}^{-\mathrm{j}2\pi\cdot\Delta\hat{f}_n[p]\cdot t_{\mathrm{s}}^{\ell}[k']}\right\} \tag{26}$$

Once these steps are performed, all errors have been estimated: $\Delta\hat{t}_{n\to 0}[p]$, $\Delta\hat{f}_n[p]$, $\Delta\hat{\varphi}_n[p]$.

C. Transfer of estimated drifts to the radar channels

After the three estimates have been obtained, they need to be applied to the radar echo data. For this, one can use reinterpolation for the correction. The obtained difference

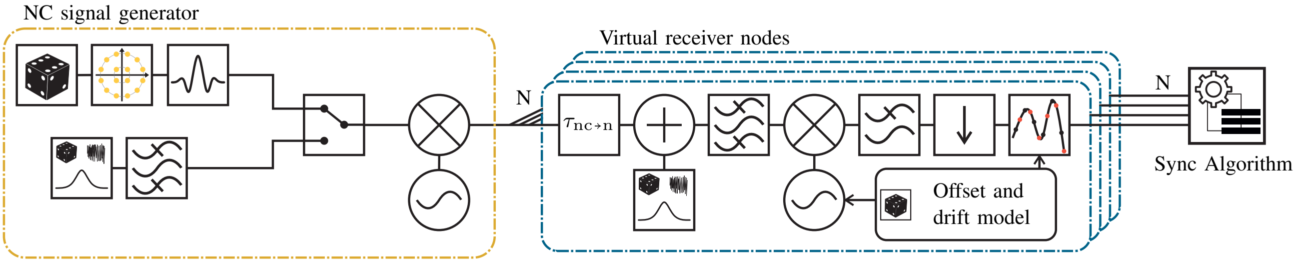

Fig. 2: Data flow path for the simulation framework. The NC signal generator can be selected to generate modulated carriers or noise signals. All connecting receiver nodes add white Gaussian noise and perform non-ideal frequency conversion and time re-interpolation. The simulation framework was programmed to be highly parallelized with pipelining for efficient data transfer.

estimates in time, frequency and phase are valid for the NC signal record start times at the base node $t^{\ell}_{0,\mathrm{s}}$. Meaning, the differences capture an event in time that does not necessarily coincide with the radar data echo record times $t^{\ell}_{0,\mathrm{s,radar}}$. However, as the local clock record times of all nodes are known, they can be easily re-interpolated, using first or second order polynomial interpolation methods, applied over a sliding window of a few PAIs. Here, linear interpolation over 2 PAIs is used.

As this realization uses the same LO signal for both receiver chains, the phase correction only needs to be interpolated to the correct timestamps. However, if in a realization this requirement could not be met, the reinterpolation for the correction data would need to take the additional frequency offset into account. To serve as a first demonstration, this scenario is outside the scope of this work.

The correction can then be easily applied to the radar echo data. The reader will have noticed, that this approach does not synchronize absolutely in time. Contributions from erroneous initial coarse computations of the propagation delay ($\tau_{\mathrm{nc}\to\mathrm{n}}$), originating from a not exactly known position of the NC signal source, will be indistinguishable from clock offsets and thus lead to range errors. As the estimated time difference contains both the path length differences $\tau_{\mathrm{nc}\to n}$ and the local time offsets, absolute range measurements are not yet possible. But as $\tau_{\mathrm{nc}\to n} = \mathrm{const}\ \forall n\ \forall t$ is assumed in this work, relative range measurements are possible. A range alignment can be performed before the image generation is performed [11]. Most importantly, all drifts are compensated and tracked, which is a necessity for the image formulation task. Notably, a high-resolution radar imaging application comes with its own challenges such as a good position information for each sensor. But as we want to emphasize this work to the synchronization aspect, we assume those challenges to be tackled, and sufficient information is available for the image formulation process.

The complete steps can be summarized by Algorithm 1.

Algorithm 1 Synchronization algorithm for node n to base node 0

```
Input: $\mathbf{R}_n[p,m], \mathbf{R}_0[p,m]$
Output: $\Delta\hat{t}_{n\to 0}[p],\ \Delta\hat{f}_n[p],\ \Delta\hat{\varphi}_n[p]$
for $p = 0$ to $P-1$ do
    $\Delta\hat{t}_{n\to 0}[p]$ = perform estimator from III-A between $\mathbf{R}_n[p,:]$ and $\mathbf{R}_0[p,:]$
    $\boldsymbol{R}_{n,\leftrightarrow}[p,:]$ = shift $\mathbf{R}_n[p,:]$ by $\Delta\hat{t}_{n\to 0}[p]$
    clear cyclically shifted samples from $\boldsymbol{R}_{n,\leftrightarrow}$
end for
$\boldsymbol{S}_n[p,m] = \boldsymbol{R}_0[p,m] \odot \overline{\boldsymbol{R}}_{n,\leftrightarrow}[p,m]$
$s_n[k] = \boldsymbol{S}_n\left[\left\lfloor \frac{k}{K} \right\rfloor, k \bmod K\right]$
$\Delta\hat{f}^{(0)}[p] = f^{\ell}_{\mathrm{LO}} \cdot \nabla\Delta\hat{\boldsymbol{t}}_{n\to 0}$
let $\mathscr{R} = \left[\Delta\hat{f}^{(0)} - \frac{\mathrm{PRF}^{\ell}}{2}, \Delta\hat{f}^{(0)} + \frac{\mathrm{PRF}^{\ell}}{2}\right)$
for $p = \lfloor (W-1)/2 \rfloor$ to $P - 1 - \lfloor (W)/2 \rfloor$ do
    $\mathscr{K}_p = \{K \cdot (p - \lfloor (W-1)/2 \rfloor), \ldots, K \cdot (p + \lfloor W/2 \rfloor)\}$
    $\mathscr{P}_p(f) = \sum_{k' \in \mathscr{K}_p} s_n[k'] \cdot \mathrm{e}^{-\mathrm{j}2\pi \cdot f \cdot t^{\ell}_{\mathrm{s}}[k']}$
    $\Delta\hat{f}_n[p] = \arg\min_{f \in \mathscr{R}} \left\{ \frac{-1}{WK} \left|\mathscr{P}p(f)\right|^2 \right\}$
    $\Delta\hat{\varphi}_n[p] = \angle \left\{ \sum_{k' \in \mathscr{K}_p} s_n[k'] \cdot \mathrm{e}^{-\mathrm{j}2\pi \cdot \Delta\hat{f}_n[p] \cdot t^{\ell}_{\mathrm{s}}[k']} \right\}$
end for
Interpolate $\Delta\hat{t}_{n\to 0}[p],\ \Delta\hat{f}_n[p],\ \Delta\hat{\varphi}_n[p]$ from $t^{\ell}_{0,\mathrm{s}}$ to $t^{\ell}_{0,\mathrm{s,radar}}$
```

IV. SIMULATIVE STUDIES

In order to test and quantify the synchronization scheme, a simulation framework was developed and used for extensive testing. For this, a NC signal was needed to be computed and received at N virtual radar nodes. To validate the presented procedure, two types of NC signals were tried. As the synchronization algorithm relies on the random characteristics of the NC signal, a band-limited Gaussian noise signal as well as a broadband modulated signal were tried. The flow diagram of the simulation data can be seen in Fig. 2. From the NC signal generator, which is able to produce both types of signals, the signal is duplicated and given to N virtual receiver nodes. These virtual receiver nodes, add white Gaussian receiver noise, filter and mix the signal into the baseband using non-ideal frequency conversion and resample the signal in congruence with their local clock offsets and drifts.

A. Simulative NC signal generation

As a first type, a multi-carrier (MC) satellite TV transponder DVB-S2 signal was created by (27) according to the signal definition [27]. The signal generated can be described by

$$s_{\mathrm{nc}}(t) = \sum_{c=-C/2}^{C/2} m_c(t) \cdot \exp(\mathrm{j}2\pi c\,\Delta f_{\mathrm{sub}} t) \cdot \exp\left(\mathrm{j}2\pi f_{\mathrm{nc,c}} t\right) , \tag{27}$$

where $m_c(t)$ is the complex pulse-formed baseband signal of subcarrier c (of C total carriers) with an underling random 16-APSK symbol sequence, a subcarrier frequency spacing of Δf_{sub} and the overall carrier frequency $f_{\mathrm{nc,c}}$ to be in accordance with (4). The overall signal carrier frequency was set to be at 11.5 GHz. For this study, the subcarrier spacing was set to $\Delta f_{\mathrm{sub}} = 31\,\mathrm{MHz}$ and a symbol rate of 22 MSym/s with a total of $C = 15$ sub-carriers were modeled. The parameters were chosen such that this signal could be generated in the laboratory for preliminary experiments as well (Section V-A2).

The second NC signal tried is a Gaussian noise signal. It is band-limited with a Hamming filter to a 10 dB bandwidth of 350 MHz, to be comparable to the MC modulated signal and the upcoming laboratory experiments.

B. Virtual receiver nodes

At the virtual radar nodes a local random Gaussian white noise vector is added to the NC signal from (27) and down converted by a LO signal as modeled in (3). The phase noise realization ς_n was created for each station in accordance with the modelling in [28] and the initial phase was randomly selected from a uniform distribution for each node $\varphi_{n,0} \sim \mathcal{U}(-\pi, \pi)$. For simplicity, a constant but random offset frequency ($f_{n,\mathrm{LO}} \sim \mathcal{U}(f_{0,\mathrm{LO}} \pm 5\,\mathrm{PPM})$) plus the phase noise realization was modeled. The signal is then filtered, decimated and re-interpolated to the simulated non-ideal timing grid of the local node, before all signals are fed into the presented algorithm. One of the simulated nodes is denoted as the base-node, while the others are treated as remote nodes.

The simulator makes a few idealized assumptions, which need to be justified. Firstly, as the frequency estimator is memoryless outside the sliding window W and multiple statistically independent nodes are simulated, it is evident, that any frequency offset can be synchronized, and slow frequency drifts are validated by the simulator. Secondly, the timing estimation relies on a nonlinear least-squares approach using a sinc function kernel. That this assumption is valid, can be seen in Fig. 3 where the cross-correlation function of two simulated baseband signals is depicted. It is evident, that peak finding with the sinc function kernel is an appropriate choice in this case. As the timing estimation with the nonlinear least-squares approach is already demonstrated in [24], the simulations shown here are only demonstrating the introduced frequency and phase estimation step. The total working scheme, with time, frequency and phase estimation is presented with the real world measurements in Section V.

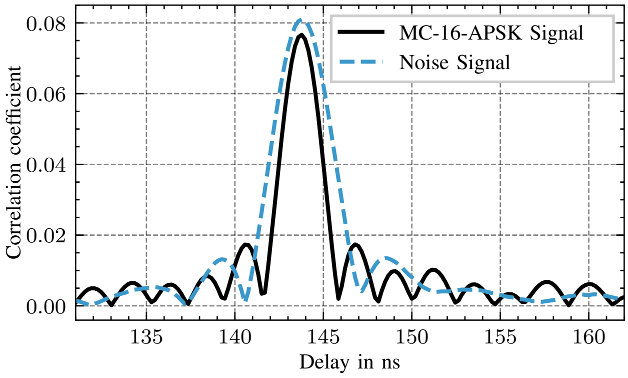

Fig. 3: Cross-correlation function between a virtual receiver node and the virtual base node for both simulated NC signal types.

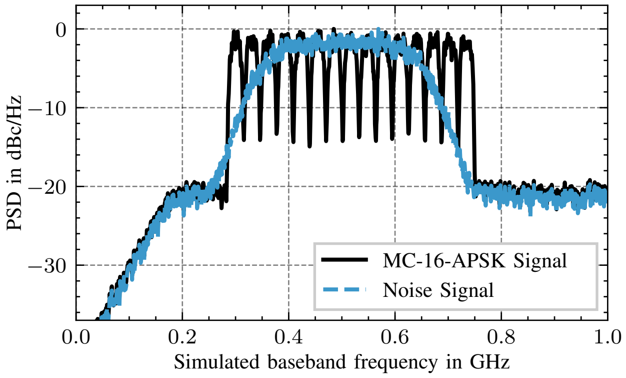

Fig. 4: Simulated PSD of both signal types at the baseband level used as input for the synchronization algorithm.

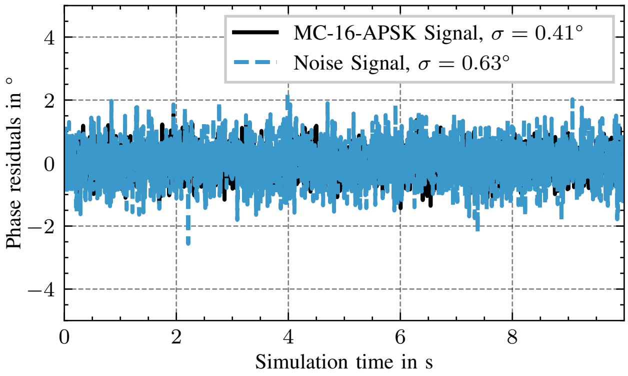

Fig. 5: Simulated phase residuals for the frequency and phase estimation step with an signal-to-noise ratio (SNR) of 20 dB and two different signal types.

C. Simulation results

Once a simulation is run, the results of the synchronization algorithm can be checked against the true values. The simulation framework stores the drifts in timing and phase as well as the algorithmic output, allowing the residuals to be checked in the evaluation phase. A simulation example with 20 dB SNR is shown in Fig. 4, where the PSD at a receiver node is shown for both evaluated signal types. For the simulation, a PAI duration of 50 µs is configured, and a window for estimation of

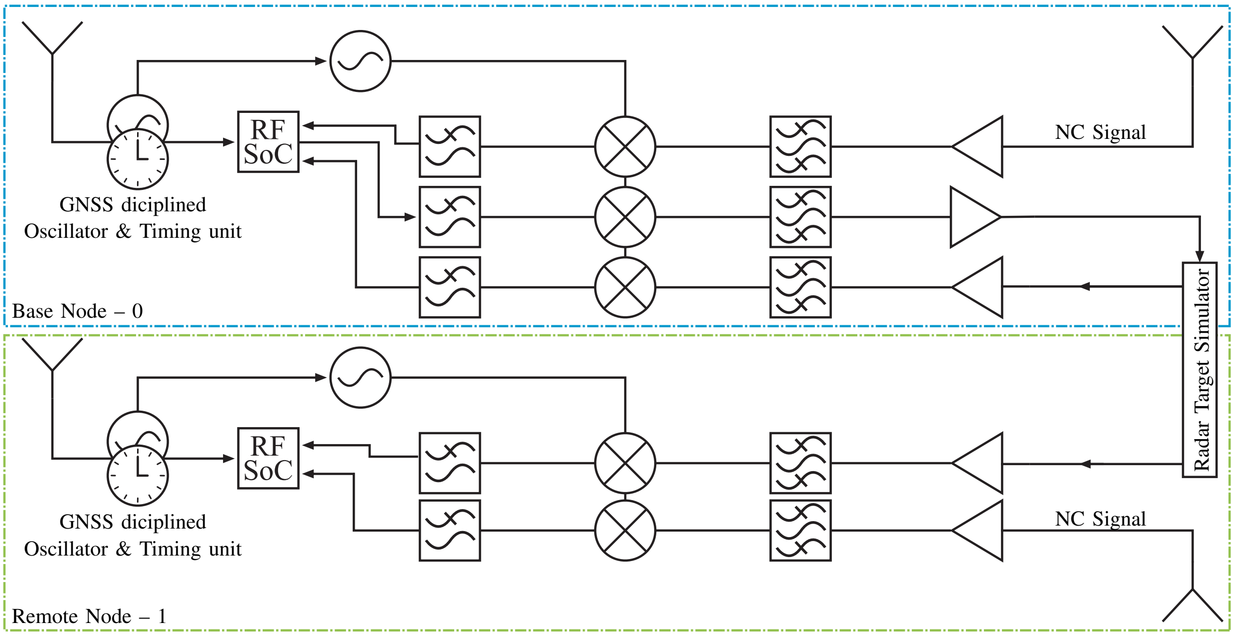

Fig. 6: Block diagram of the experimental setup, with the base node denoted in blue (top) and the remote node marked in green (bottom). The analog-to-digital converters (ADCs) and digital-to-analog converter (DAC) are integrated within the RF-SoC. The antennas of the NC signal receivers were pointed towards the ASTRA TV broadcast satellite and the target simulation was implemented with a true time-delay. Each node operates on its own GNSS-diciplined time base and within one node only one LO signal is used for all mixers in that node.

$W = 2$ is used. The phase residuals, which are the per pulse differences between the corrected signal phase and its true phase, are shown in Fig. 5. As can be seen, there remains no drift in the corrected data, giving confidence that the presented algorithm works as intended.

Moreover, both signal types present residuals with a 1σ standard deviation of less than $1°$, presenting tight phase coherence in X band using only NC signals. The phase residuals also pass the Shapiro-Wilk test for normality with a p value of $p = 0.20$ for the MC modulated signal and $p = 0.69$ for the noise signal [29]. This gives confidence that the estimation steps are able to estimate the deterministic signal components and only Gaussian noise remains.

It can be seen that the MC modulated signal exhibits a lower variance in the residuals compared to the noise signal. This effect can be explained by the occupied bandwidth of the signals used for estimation, depicted in Fig. 4. As there is more energy in the edges of the band, the estimation variance is lowered [25, Chapter 3.5] [30].

It can be concluded, that a wide bandwidth and high SNR NC signal promises a tight phase coherence. A simplified drift and phase noise model promises less than $1°$ of phase variation when signals with 20 dB SNR and a bandwidth of more than 350 MHz are used. The initial test will be performed on the total transponder of a broadcast television (TV) satellite, thus allowing these conditions to be met and giving confidence in our new interpretation into synchronization using NC signals.

V. EXPERIMENTAL VERIFICATION

To verify the proposed synchronization scheme, an experimental hardware system was built with a total of two nodes to test the feasibility of the proposed synchronization scheme. A schematic block diagram can be seen in Fig. 6. The main component is the RF system on a chip (SoC) used for digital sampling and timing. All sampling rates were set to 4.9 GHz. The base station, denoted with the index 0, is equipped with a radar transmitter able to generate wide-bandwidth modulated signals suitable for high resolution imaging radar applications. In this demonstration, the transmit waveform was a linear frequency modulated (LFM) chirp signal with a chirp duration of 25 µs and a bandwidth of 2.2 GHz. The pulse-repetition frequency (PRF) was set to 250 Hz. More so, both the remote unit, and the base unit are equipped with radar receivers and receivers for the NC signal. As target simulation, a true time delay line was used. This highly idealized target simulation can be used to verify the synchronization degree, as the remaining timing and phase error can be easily extracted by the singular stationary virtual target. To verify the proposed scheme, the radar and NC signal reception channels were set to operate concurrently, as only in this case, the true estimation residuals can be obtained by the radar data.

For the indoor laboratory experiments, the NC signal was a MC modulated 16-APSK signal, similar to the DVB-S2 signals emitted by geostationary broadcast TV satellites. For the outdoor experiments, the NC signal was chosen to be the DVB-S2 signal from the geostationary ASTRA satellites at 19.2° E [31]. The base clock at both nodes was derived from a low noise rubidium GNSS-disciplined frequency standard, meaning no long term drift is expected [32]. This frequency standard was used as the reference for the base clock and sampling rates. It is also the reference for the LO generation operating at 11 GHz used in the frequency conversion stage

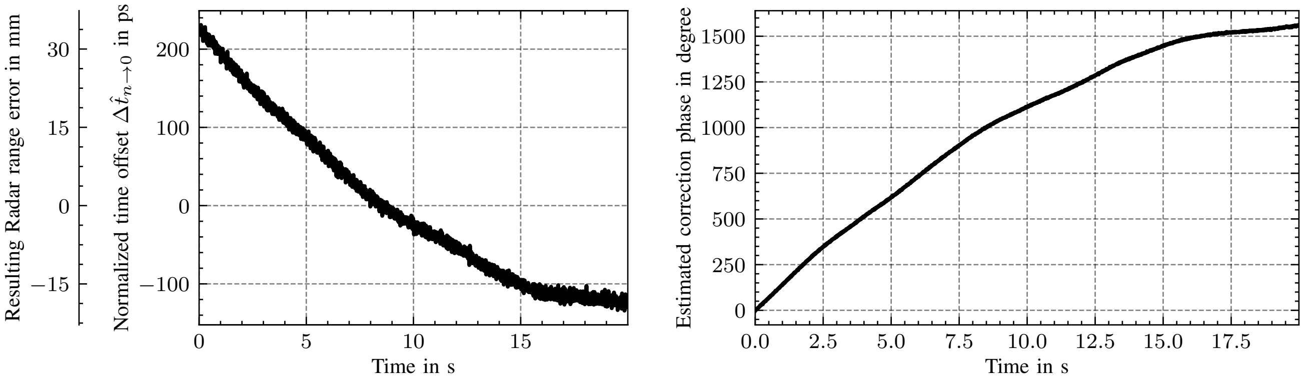

(a) (b)

Fig. 7: Results from the indoor measurement with the timing and resulting range drift results in (a) and the unwrapped estimated phase drift $\Delta\hat{f}_n t^{\ell} + \Delta\hat{\varphi}_n$ in (b). In (a) the median of −11.72 ns was removed to clearly show the drift.

of all receivers and the transmitter within a single node. This reference is removed for the measurement presented in Section V-B2, to show the robustness of the synchronization approach.

A. Laboratory experiments

Before real-world outdoor measurements using true NC signals can be conducted, the system needs to be validated in a first and simplified manner. Firstly, the initial synchronization using the GNSS-diciplined base clocks are verified, and then, in a secondary step, indoor experiments are conducted using artificially and controlled NC signals. Thirdly, the measurements were conduced outdoor using true NC signals to demonstrate the proposed scheme.

1) Preliminary laboratory experiments: As the presented scheme is used for fine synchronization in time and phase, it relies on a coarse initial synchronization, such that the reception windows overlap sufficiently. To verify the remaining timing drift using the GNSS-dicipined oscillators as a base clock, a reduced experiment was conduced. The systems from Fig. 6 were connected in the baseband, without any frequency conversion stages in the loop. This way, the pure timing errors from the systems can be tracked. A result can be seen in Fig. 8, where the clock offsets are visualized over a time span of 10 min. As can be seen a swing of approximately 5 ns with a clock offset of 119 ns can be observed. The observed values coincide with the expected synchronization accuracy of GNSS-based methods. Thus, the majority of the reception window of 30 µs are overlapping in time and can be used for estimation. The behavior is as expected from GNSS-diciplined oscillators and shows no large drift that would hinder the coordinated reception.

2) Laboratory experiments using artificial NC signals: To validate the synchronization scheme, an indoor experiment was conducted. The NC signal was output from a vector signal generator with the signal power set such that the resulting SNR at the ADCs is about 13 dB for the base node and 11 dB for the remote node. The difference in the observed SNR levels can be explained by different cable lengths and corresponding losses. As a NC signal, 15 parallel carriers with a carrier spacing of 31 MHz, each with a random 16-APSK symbol sequence at a rate of 22 MSym/s and root-raised cosine pulse form were used. The carrier frequency of the NC signal was set to 12.4 GHz. In total 5000 pulses with a PRF of 250 Hz, so a total measurement duration of 20 s, was recorded.

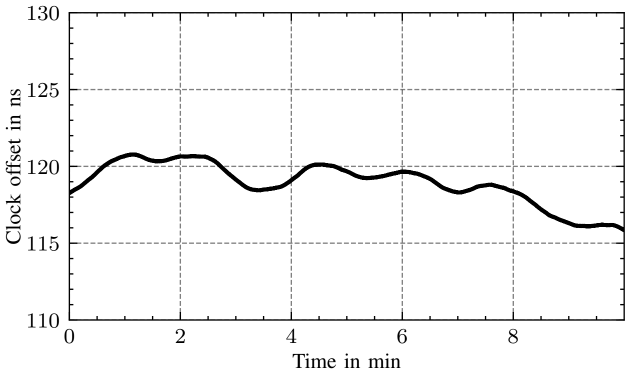

Fig. 8: Measurement of uncorrected GNSS-diciplined system clocks.

After the measurement, Algorithm 1 was performed and the correction was applied to the radar channel. Figure 7a shows the normalized timing offsets obtained by the NC channel and Fig. 7b shows the estimated combined correction phase and frequency to be applied to the radar channel. After this has been applied, the residual timing error and phase after pulse compression can be seen in Fig. 10.

In Fig. 7 the errors can be seen, that would occur without the presented fine synchronization. Those drifts in time and phase are unacceptable for high resolution imaging radar applications, targeting coherent multistatic operation in the single-digit centimeter resolution regime. Although the oscillators are disciplined using GNSS, a phase offset of more than 360° is observed after just 2.5 s. The focusing of an ISAR

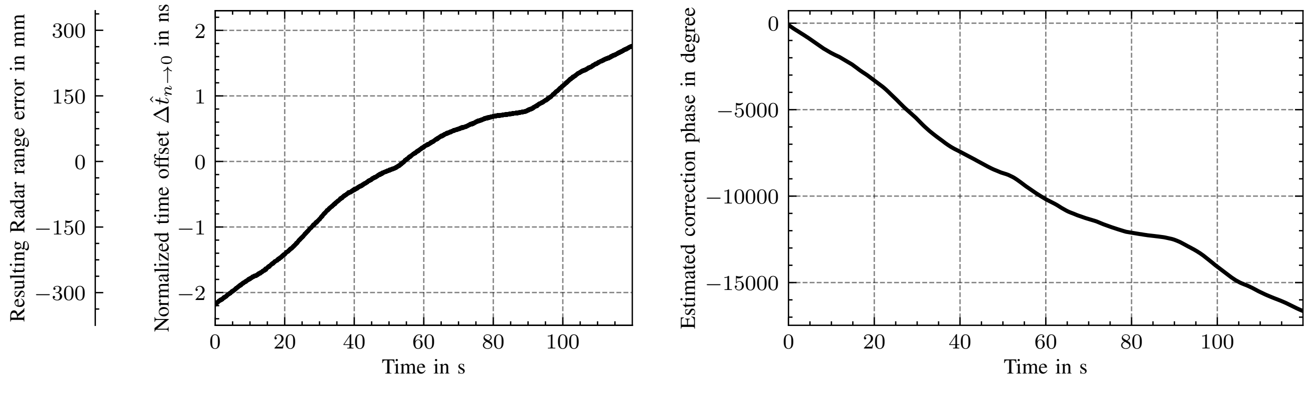

(a)

(b)

Fig. 9: Results from the outdoor measurement with the timing and resulting range drift results in (a) and the unwrapped estimated phase drift $\Delta\hat{f}_n t^{\ell} + \Delta\hat{\varphi}_n$ in (b). In (a) the mean of −129.4 ns was removed to clearly show the drift.

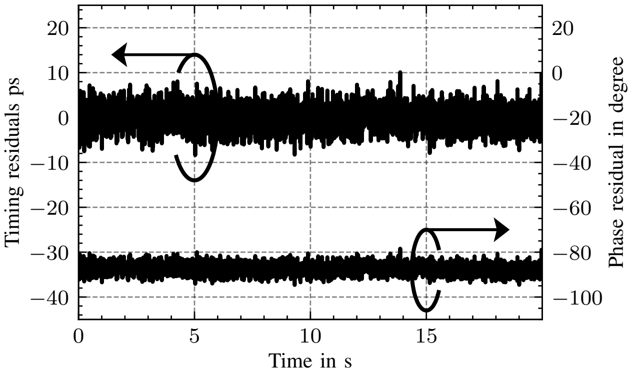

Fig. 10: Timing and phase residuals of the indoor measurement obtained via the radar receiver after the correction based on the NC signal processing has been applied.

image would not be possible for such a phase drift. This further demonstrates the need for accurate synchronization techniques in distributed SAR systems operating at a high center frequency.

With the correction applied, the timing residuals have a 1σ deviation of 2.45 ps and a 1σ phase deviation of 2.18° is observed. Both residuals from Fig. 10 were tested against normality using the Shapiro-Wilk test [29]. The timing residuals passed the normality test with $p_{\Delta\hat{t}_{n\to0}} = 0.657$ and the phase residual passed with $p_{\Delta\hat{\varphi}} = 0.737$ giving strong confidence, that the assumed signal model is valid and after the estimation process only white Gaussian noise remains. These measurements are in accordance with the simulation results presented here. However, the discrepancy in the phase estimation variance can be mostly explained by the simplified drift and oscillator noise model in the simulator.

B. Outdoor experiments

After the lab experiments were successfully conducted, an outdoor measurement followed. As mentioned above, the lab-generated NC signal was swapped for the true satellite broadcast TV signal from the ASTRA satellite. This outdoor hardware experiment can be seen in Fig. 11. The hardware was set up on a singular physical platform and held electrically in two separate nodes. For the receiving antennas two 70 cm commercial off-the-shelf (COTS) offset reflector antennas were used, separated by a small baseline of 2.60 m. Modified

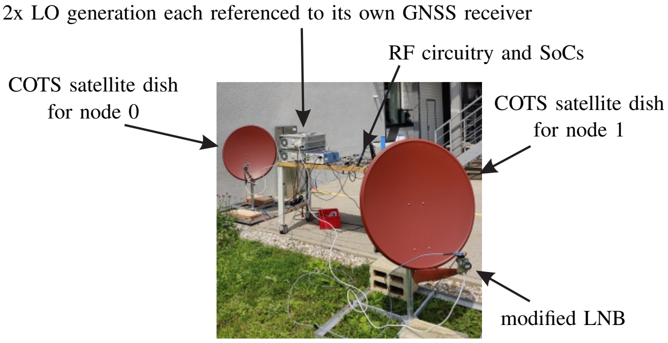

Fig. 11: Overview photo of the outdoor measurement setup. Although both nodes are mounted on the same physical platform, they are wired and configured to operate as two nodes as described in Fig. 6.

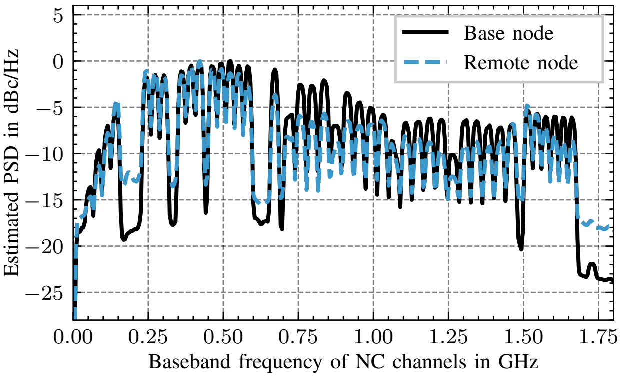

Fig. 12: Estimated PSD of the outdoor measurement using the ASTRA broadcast satellite as the NC signal source in the baseband used for estimation. A SNR of 16.5 dB and 10.3 dB for the base and remote channel respectively are measured.

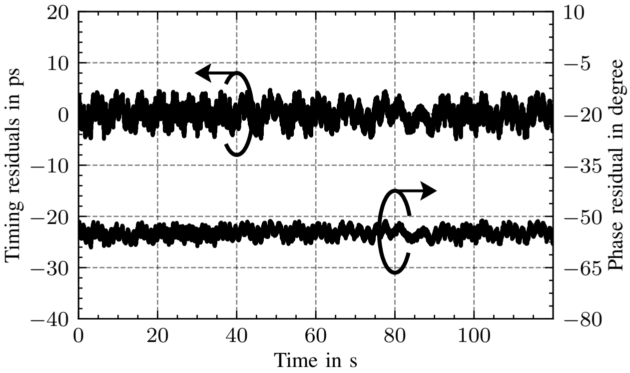

Fig. 13: Timing and phase residuals of the outdoor measurement obtained via the radar receiver after the correction based on the NC signal processing has been applied.

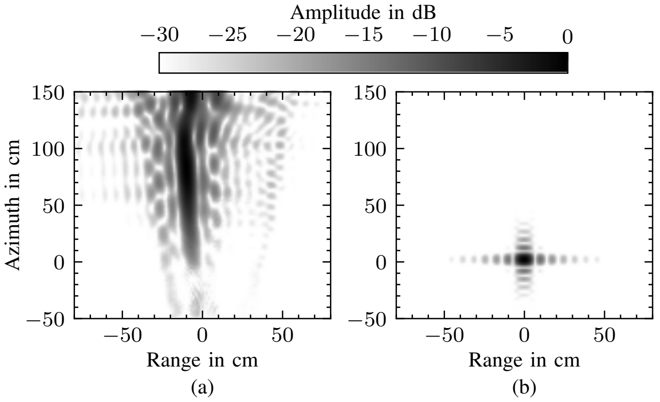

(a)

(b)

Fig. 14: Virtually focused ISAR images based on the radar echos of the outdoor measurement in (a) without the synchronization and in (b) after the radar data has been synchronized using the correction values obtained through the NC signal.

consumer satellite receiver low-noise block downconverters (LNBs) were used to feed the RF signal from the antennas to the receivers. The resulting SNR at the ADCs was measured to be 16.5 dB and 10.3 dB for the base and remote node respectively, and the estimated PSD can be seen in Fig. 12.

As can be seen, the total transponder bandwidth of about 1.75 GHz is available for estimation, which is significantly higher than the previously shown results, however at also different SNR levels. The reception time was set to 30 µs.

1) Experiments using the proposed scheme: To validate the proposed scheme, 12 000 pulses with a PRF of 100 Hz were recorded. Fig. 9 shows time and coherence estimates obtained by the ASTRA broadcast signal. After this correction data has been applied to the radar channels, the pulse-compressed peak in time and phase can be evaluated and interpreted as residuals. Those can be seen in Fig. 13, where both the timing and phase residuals are shown. The 1σ timing deviation is observed at 1.71 ps and the 1σ phase deviation is observed at 1.33°.

The given deviations are 1.12 ps and 0.85° lower than residuals obtained in the laboratory experiments. This can be explained by the higher bandwidth transmitted by the satellite compared to lower bandwidth of 500 MHz available when using the vector signal generator. However, as the residuals do not pass the statistical test for normality, there are deterministic effects present. The origin is yet unknown, but this also renders any comparison to the theoretical Cramér–Rao lower bound (CRLB) irrelevant, as estimators' residuals are not pure noise [25, Chapter 3]. However, the residuals are low enough to allow high resolution imaging techniques to be employed.

To demonstrate this, it is possible to virtually focus the received radar data into an ISAR image of an ideal point target. This can be seen in Fig. 14 where two virtually generated ISAR images can be seen. On the left-hand side, the uncorrected pulse compressed radar echo data is tired to be focused. As can be seen, the focusing in azimuth is virtually not possible due to the observed phase drift between the two nodes. Also, a smearing in range can be observed, which is significantly large. This emphasizes the fact that regular GNSS-diciplined oscillators, which serve at the nodes as timing and phase references, cannot be used in high-resolution imaging tasks – at least not in X band. On the right-hand side however, the same radar echo data was focused, and each pulse was corrected by the correction values obtained by the NC signal. As is expected by the residuals discussed previously, here an ideal point target can be focused, promising that this synchronization scheme enables high-resolution imaging.

2) Experiment using free-running local oscillators: To further test the resilience of the presented synchronization scheme, a second experiment was conducted. For that, the reference coupling from the LO signal to the GNSS-diciplined station clock was removed, such that the LO signals in the mixing stages were allowed to drift freely. Then, the measurement was repeated using a higher PRF of 500 Hz for a total measurement duration of 12 s. As in such a case the timing drifts have no correlation to the LO drifts, (20) does not hold. To evaluate the measurement anyway, the initial frequency offset of $\Delta\hat{f}^{(0)} = 0$ was assumed, with the notion, that the higher PRF captures the true frequency offset. The obtained results are shown in Fig. 15, where the timing and phase estimates are plotted. That the LO signals have a significant frequency offset can be observed in Fig. 15b, where the linear phase drift (constant frequency offset) of 115.7 Hz can be seen. As the reference was removed, this large offset is expected. But as the offset was obtainable by the NC signal, the error residuals can be computed and are shown in Fig. 16. As can be seen, the phase and timing drifts are completely removed, and a timing 1σ standard deviation of 1.75 ps and a phase deviation of 1.21° are observed. Thus promising an X-band radar to produce focused images suitable for multistatic applications. In contrast to the indoor experiments using the artificially generated NC signals, those residuals also do not pass the statistical test for normality, although the human eye might interpret Fig. 16 differently. As different parameters were used in this experiment, the time axis is scaled differently, hiding the deterministic effects from being visible in Fig. 16 compared to Fig. 13. However, the expected reduction of the estimation variance compared to the indoor experiments are nevertheless observed, thus being a valid proof-of-concept and promising our novel idea to be usable.

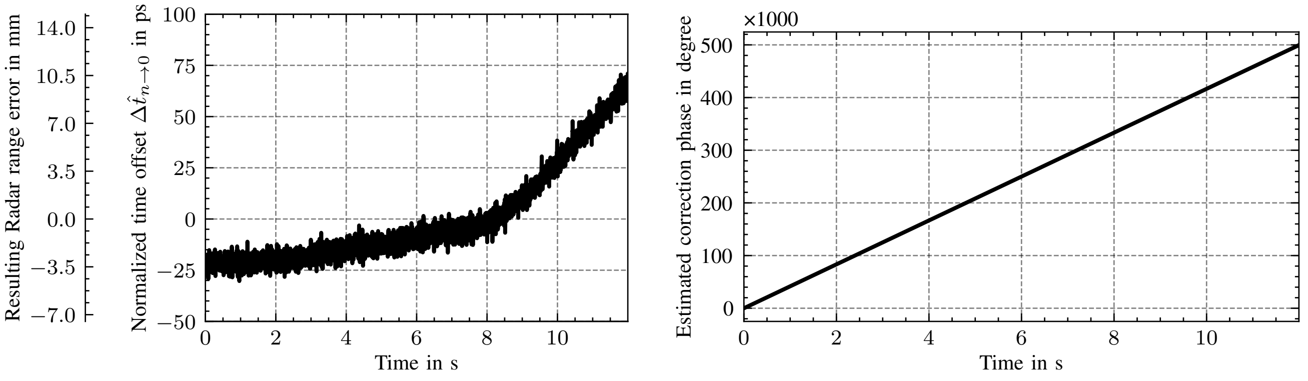

(a) (b)

Fig. 15: Results from the outdoor measurement using the free-running oscillators with the timing and resulting range drift results in (a) and the unwrapped estimated phase drift $\Delta\hat{f}_n t^{\ell} + \Delta\hat{\varphi}_n$ in (b). In (a) the mean of 3.8 ns was removed to clearly show the drift.

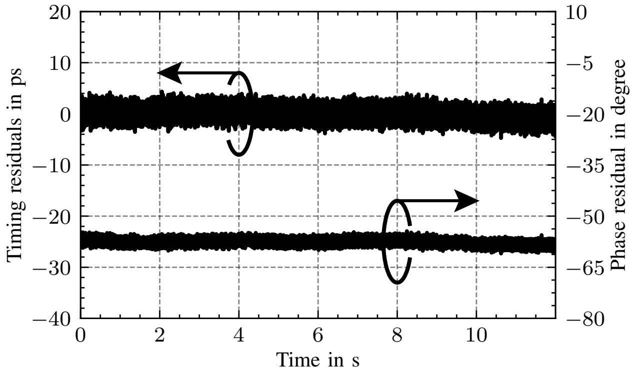

Fig. 16: Timing and phase residuals of the outdoor measurement using the free-running oscillators obtained via the radar receiver after the correction based on the NC signal processing has been applied.

VI. CONCLUSION

In this work, a novel synchronization scheme was proposed using non-cooperative signals of arbitrary origin. The synchronization scheme was analyzed in simulations and verified using a demonstrator using a broadcast satellite TV signal for synchronization. Without imposing too strict requirements on the NC signal, a synchronization timing error of about 1.75 ps and a phase synchronization of less than 1.33° for an X-band imaging radar can be achieved, which is with regard to timing about three orders of magnitude better than regular GNSS-based synchronization. Unlike other synchronization methods, our high-accuracy synchronization is achieved in the post-processing stage of the radar application, meaning the high degree of precision of our proposed scheme is not physically present in the hardware during runtime. This renders our approach cost-effective, as only an additional receiver chain needs to be set up at all participating nodes, and no expensive specialized components are needed. Although the experimental setup demonstrates the synchronization of a single remote receive only node, the approach is easily adaptable to arbitrary many remotes. As the algorithm is executed pairwise (remote node n to the base node 0) to calculate the correction, the computational effort scales with $\mathcal{O}(N)$.

The NC signal used in this work is the satellite broadcast TV signal emitted by the geostationary ASTRA satellites. As whole transponder signal with a bandwidth of about 1.75 GHz is used for the synchronization purpose, and these signals can be received with high SNR, this high degree of synchronization can be achieved. Also, as we are focusing on the oscillator phase, this new approach can be used for multistatic ISAR systems operating coherently for interferometric or tomographic imaging tasks. Furthermore, it is demonstrated, that this technique can synchronize datasets obtained by using free-running oscillators without being referenced to the stations clock, giving design-freedom to the oscillators in use, which is also new feature of our method. This demonstrates, that the achievable result is independent of the PLL realization and loop-filter. In general, the simulative results agree well with the measured real-world data, allowing our system to be deployed.

Although the presented synchronization accuracy captures all drift components and synchronizes the remote nodes to a satisfactory degree of accuracy, the real-world measurements have shown that, when using real NC signal, the residuals exhibit deterministic effects of yet unknown origin. The residuals only pass the statistical test for normality when operating in a controlled laboratory environment. Further investigations are needed, and, if the origin were to be found, a much lower estimation variance would result. This would elevate the synchronization accuracy further, enabling research into multistatic ISAR systems operating at even higher center frequencies.

Furthermore, a detailed investigation into the decorrelation effects of the NC signals needs to be addressed in the future to verify larger separations of the participating nodes. This includes investigations into atmospheric effects, weather dependencies, multipath effects and availability analysis for a multitude of NC signal sources. Especially since a rough position estimate of the NC signal source is needed to operate this scheme with large baseline separations successfully, this limits the choice of signal sources usable for this scheme. Moreover, the current model assumes a stationary scenario, whose validity is not true for all NC signal sources. Operating this scheme at larger baseline lengths will increase its sensitivity for dynamic scenarios, which will need to be investigated in the future. Additionally, the signal propagation from the NC signal source to the respective nodes was considered to be LOS, neglecting possible multipath effects. Although this simplification should be valid for our demonstrated use case, where we are able to employ high gain antennas targeting a constant illuminator, it is certainly not valid for all scenarios. If it were possible for the base station to obtain a clean NC signal to serve as a reference, a channel estimation for the remote nodes should be possible, and, given further detailed analysis, an extension to multipath scenarios could be possible. After the presented proof-of-concept, we set the necessary foundation for further studies promising IoSiS-NG a synchronization method for multistatic imaging of satellites in space.

ACKNOWLEDGMENTS

The authors would like to acknowledge the support of the workshop and team members who assisted with conducting experiments.

A patent application about the presented synchronization scheme has been filed with the German Patent and Trade Mark Office (Application No. 10 2025 124 272.0).

APPENDIX
EFFECTS OF REAL WORLD SAMPLING RATE ERRORS

A system, which bases its sampling rate on GNSS-disciplined oscillators, will exhibit no average median drift in their offset. We observed a short-term maximum drift between two disciplined clock oscillators of about 100 ps/s. During a single acquisition within one pulse of 30 µs, our two systems drifted apart by 3 fs, meaning the acquisition of one system was about 3 fs longer than the other. Because the PLL's timing jitter is specified to be in the range of 100 fs, we can safely assume that, that during a single acquisition interval, both systems are operating on the same sampling frequency, as the jitter noise is orders of magnitudes larger than the drift introduced speed-up or slow-down of the sampling frequency. Correcting this effect can be neglected within a single PAI, and the timing drifts are only observed on a PAI to PAI basis.

REFERENCES

[1] G. Krieger and A. Moreira, "Multistatic sar satellite formations: Potentials and challenges," in *Proceedings. 2005 IEEE International Geoscience and Remote Sensing Symposium, 2005. IGARSS '05.*, vol. 4. Seoul, Korea: IEEE, 2005, pp. 2680–2684.

[2] A. Moreira, G. Krieger, I. Hajnsek, K. Papathanassiou, M. Younis, P. Lopez-Dekker, S. Huber, M. Villano, M. Pardini, M. Eineder, F. De Zan, and A. Parizzi, "Tandem-L: A Highly Innovative Bistatic SAR Mission for Global Observation of Dynamic Processes on the Earth's Surface," *IEEE Geoscience and Remote Sensing Magazine*, vol. 3, no. 2, pp. 8–23, Jun. 2015.

[3] J. Kanz, C. Bonfert, C. Gesell, A. Grathwohl, F. Bormuth, G. Krieger, and C. Waldschmidt, "Coherent Multistatic UAV-Based SAR," *IEEE Transactions on Radar Systems*, pp. 1–1, 2025.

[4] M. Villano, M. N. Peixoto, S. Kim, V. M. Pérez, N. Ustalli, J. Mittermayer, T. Börner, G. Krieger, and A. Moreira, "Potential of Multi-Static SAR Systems for Earth Monitoring and Their Demonstration Using Swarms of Drones," in *IGARSS 2023 - 2023 IEEE International Geoscience and Remote Sensing Symposium*, Jul. 2023, pp. 4586–4589.

[5] M. Martorella, J. Palmer, J. Homer, B. Littleton, and I. D. Longstaff, "On Bistatic Inverse Synthetic Aperture Radar," *IEEE Transactions on Aerospace and Electronic Systems*, vol. 43, no. 3, pp. 1125–1134, Jul. 2007.

[6] M. Younis, R. Metzig, and G. Krieger, "Performance Prediction of a Phase Synchronization Link for Bistatic SAR," *IEEE Geoscience and Remote Sensing Letters*, vol. 3, no. 3, pp. 429–433, Jul. 2006.

[7] S. Dunkel and E. Schreiber, "Phase Synchronization Concept for the Bistatic Extension of the Airborne F-SAR System," in *2024 Kleinheubach Conference*, Sep. 2024, pp. 1–4.

[8] J. Tian, Y. Cheng, N. Xie, and D. Hou, "Bistatic ISAR imaging based on phase synchronization with fiber optic link," in *2016 IEEE Radar Conference (RadarConf)*, May 2016, pp. 1–5.

[9] P. Lopez-Dekker, J. J. Mallorqui, P. Serra-Morales, and J. Sanz-Marcos, "Phase and temporal synchronization in bistatic SAR systems using sources of opportunity," in *2007 IEEE International Geoscience and Remote Sensing Symposium*, Jul. 2007, pp. 97–100.

[10] A. Theodosiou and P. López-Dekker, "Data-driven Phase Synchronization of Harmony's Ocean Surface Topography Product," *IEEE Transactions on Geoscience and Remote Sensing*, pp. 1–16, 2025.

[11] M. Rodriguez-Cassola, P. Prats-Iraola, P. Lopez-Dekker, A. Reigber, G. Krieger, and A. Moreira, "Autonomous time and phase calibration of spaceborne bistatic SAR systems," in *EUSAR 2014; 10th European Conference on Synthetic Aperture Radar*, Jun. 2014, pp. 1–4.

[12] M. Rodriguez-Cassola, E. R. Silva Filho, P. Prats, G. Krieger, and A. Moreira, "A Robust Data-Based Clock Synchronisation Algorithm for Multi-Channel SAR Systems," in *IGARSS 2023 - 2023 IEEE International Geoscience and Remote Sensing Symposium*, Jul. 2023, pp. 7852–7855.

[13] D. Tagliaferri, M. Manzoni, M. Mizmizi, S. Tebaldini, A. Virgilio Monti-Guarnieri, C. Maria Prati, and U. Spagnolini, "Cooperative Coherent Multistatic Imaging and Phase Synchronization in Networked Sensing," *IEEE Journal on Selected Areas in Communications*, vol. 42, no. 10, pp. 2905–2921, Oct. 2024.

[14] E. Busley, T. Žuntar, J. Borgmann, and M. Krist, "Time transfer via single-record TDoA measurements of GNSS satellites using direct cross-correlation and relative pilot code phases," *IET Radar, Sonar & Navigation*, vol. 18, no. 12, pp. 2447–2453, 2024.

[15] E. Rodrigues-Silva and M. Rodriguez-Cassola, "Analysis of a POD-based Approach for Phase and Time Synchronization of Bistatic and Multistatic SAR Systems," in *EUSAR 2021; 13th European Conference on Synthetic Aperture Radar*, Mar. 2021, pp. 1–6.

[16] S. Anger, M. Jirousek, S. Dill, and M. Peichl, "High-resolution radar imaging of space objects," in *Advanced Maui Optical and Space Surveillance Technologies Conference (AMOS)*, Maui, Hawaii, Sep. 2024, pp. 506–516.

[17] T. Žuntar, E. Busley, J. Borgmann, and M. Krist, "Time Synchronization via TDoA Measurement of Broadband Satellite Signals in L-, X- and Ku-Band," in *2024 21st European Radar Conference (EuRAD)*, Sep. 2024, pp. 184–187.

[18] O. Jean and A. J. Weiss, "Passive Localization and Synchronization Using Arbitrary Signals," *IEEE Transactions on Signal Processing*, vol. 62, no. 8, pp. 2143–2150, Apr. 2014.

[19] P. Banerjee, *An Introduction to Modern Timekeeping and Time Transfer*, 1st ed., ser. Springer Series in Measurement Science and Technology Series. Cham: Springer, 2023.

[20] D. Howe, D. Allan, and J. Barnes, "Properties of Signal Sources and Measurement Methods," in *Thirty Fifth Annual Frequency Control Symposium*, May 1981, pp. 669–716.

[21] V. F. Kroupa, *Phase Lock Loops and Frequency Synthesis*, 1st ed. Wiley, Apr. 2003.

[22] A. Moreira, P. Prats-Iraola, M. Younis, G. Krieger, I. Hajnsek, and K. P. Papathanassiou, "A tutorial on synthetic aperture radar," *IEEE Geoscience and Remote Sensing Magazine*, vol. 1, no. 1, pp. 6–43, Mar. 2013.

[23] H.-J. Zepernick and A. Finger, *Pseudo Random Signal Processing: Theory and Application*. Chichester, England Hoboken, NJ: Wiley, 2005.

[24] S. Prager, M. S. Haynes, and M. Moghaddam, "Wireless Subnanosecond RF Synchronization for Distributed Ultrawideband Software-Defined Radar Networks," *IEEE Transactions on Microwave Theory and Techniques*, vol. 68, no. 11, pp. 4787–4804, Nov. 2020.

[25] S. M. Kay, *Fundamentals of Statistical Signal Processing. 1: Estimation Theory*, 20th ed. Upper Saddle River, NJ: Prentice Hall PTR, 2013.

[26] J. A. Nelder and R. Mead, “A Simplex Method for Function Minimization,” *The Computer Journal*, vol. 7, no. 4, pp. 308–313, Jan. 1965.

[27] ETSI, “Digital Video Broadcasting (DVB); Second generation framing structure, channel coding and modulation systems for Broadcasting, Interactive Services, News Gathering and other broadband satellite applications; Part 1: DVB-S2 EN 302 307-1 - V1.4.1 -,” Nov. 2014.

[28] Y. Lisong, C. Xiaolong, and W. Jiali, “A practical simulation method for generating phase noise of oscillators,” in *Proceedings of 2013 2nd International Conference on Measurement, Information and Control*, vol. 01, Aug. 2013, pp. 132–136.

[29] S. S. Shapiro and M. B. Wilk, “An Analysis of Variance Test for Normality (Complete Samples),” *Biometrika*, vol. 52, no. 3/4, p. 591, Dec. 1965.

[30] F. Harris, “On the use of windows for harmonic analysis with the discrete Fourier transform,” *Proceedings of the IEEE*, vol. 66, no. 1, pp. 51–83, 1978.

[31] “Our Coverage | SES — ses.com,” https://www.ses.com/our-coverage#/explore/orbital-position/196, accessed 2025-09-15.

[32] VIAVI Solutions Inc., “Low Noise Rubidium GNSS-Disciplined Frequency Standard,” https://www.viavisolutions.com/en-us/literature/ln-rubidium-gnss-disciplined-frequency-standard-data-sheets-en.pdf, accessed 2025-11-05.

Fabian Hochberg received the B.Sc. and M.Sc. degrees in electrical engineering and information technology from the Karlsruhe Institute of Technology (KIT), Germany in 2020 and 2023 respectively. Since 2024 he is pursuing the Ph.D. degree under the supervision of Thomas Zwick. In 2024, he joined the Microwaves and Radar Institute, German Aerospace Center (DLR), where he is currently a Research Associate, working with imaging radar, signal processing, synchronization-techniques and radar system design for multistatic space surveillance.

Matthias Jirousek was born in Gernsbach, Baden-Württemberg, Germany, in 1975. He received the Diploma degree in electrical engineering from the University of Karlsruhe (now Karlsruhe Institute of Technology KIT), Germany, in 2002 and his PhD degree in electrical engineering in 2012. His main research interests are in the development and construction of highly innovative microwave sensor system and calibration standards. Since 2003, he is affiliated with the Microwaves and Radar Institute (HR) of the German Aerospace Center (DLR), Weßling, Germany. He was responsible for research on a passive microwave imaging experimental spectrometer system based on aperture synthesis. His current research concentrates on highly digitized wideband radar instruments for imaging of satellites in space and remote sensing on high altitude platforms. He is also chief engineer for the development of precise and flexible active calibration targets for future satellite SAR calibration missions with a focus on absolute radiometric calibration. In addition, Dr. Jirousek serves as a lecturer for the KIT on space-borne microwave radiometry.

Simon Anger studied electrical engineering with a specialization in high-frequency engineering at the University of Ulm. He subsequently earned his doctorate and worked as a research associate at the Microwaves and Radar Institute of the German Aerospace Center (DLR) in the Reconnaissance and Security Department in Oberpfaffenhofen. For about 13 years, he has been engaged in high-resolution, radar-based satellite imaging and the development of innovative radar concepts for the high-precision characterization of space objects. His expertise spans the entire radar-based space surveillance imaging chain and includes ISAR image processing techniques. Currently, Dr. Anger is responsible for the experimental IoSiS (Imaging of Satellites in Space) radar system and serves as the project lead of IoSiS – Next Generation.

Markus Peichl is holding a Diploma and a PhD in Electrical Engineering, both from Technical University of Karlsruhe (now KIT – Karlsruhe Institute of Technology). He has 35 years of experience in microwave remote sensing. Joining DLR in 1990, he is leading the Microwaves Sensors Group within the Department of Reconnaissance and Security at DLR Microwaves and Radar Institute since 1998. His present interests focus on technology for space-borne, airborne, ground-based and UAV-carried microwave remote sensing systems, especially synthetic aperture radar and microwave radiometers, for a multitude of applications.

Thomas Zwick Thomas Zwick received the Dipl.-Ing. and the Dr.-Ing. degrees from the Universität Karlsruhe (TH), Germany, in 1994 and 1999, respectively. In February 2001, he joined IBM as research staff member at the IBM T. J. Watson Research Center, Yorktown Heights, NY, USA. From October 2004 to September 2007, Thomas Zwick was with Siemens AG, Lindau, Germany, managing the RF development team for automotive radars. In October 2007, he became a full professor at the Karlsruhe Institute of Technology (KIT), Germany. He is the director of the Institute of Radio Frequency Engineering and Electronics at the KIT. Since 2017 he is member of the Heidelberg Academy of Sciences and Humanities. In 2018 Thomas Zwick became appointed IEEE Fellow. In 2019, he became the Editor-in-Chief of the IEEE Microwave and Wireless Components Letters. Since 2019 he is a member of acatech (German National Academy of Science and Engineering). In 2022, he was awarded an honorary doctorate of the Faculty of Electrical Engineering and Informatics at the Budapest University of Technology and Economics in Hungary.